metals

MDPI

Article

Artificial Neural Network-Based Optimisation of Geometric Characteristics in Laser Metal Deposition of TiC/Ti6Al4V

Thabo Tlale [1,*], Peter Mashinini [1] and Bathusile Masina [1,2]

[1] Department of Mechanical and Industrial Engineering Technology, University of Johannesburg, Doornfontein, Johannesburg 2094, South Africa
[2] Photonics Centre, Manufacturing Cluster, Council for Scientific and Industrial Research, Meiring Naude Road, Brummeria, Pretoria 0001, South Africa
* Correspondence: 216077583@student.uj.ac.za

Abstract

Laser metal deposition operates on the principle of layer-by-layer material addition, wherein each layer is formed by overlapping individual single tracks. Consequently, clads formed serve as the fundamental building blocks for this technology. Their quality directly affects the overall build quality, particularly the geometric characteristics, which are also critical to process productivity. In the present work, geometric characteristics of TiC/Ti6Al4V single tracks fabricated via laser metal deposition are optimised. An artificial neural network model was developed to predict the clad width, height, and dilution using processing parameters, laser power, scan speed, and powder feed rate, as model inputs. The Particle Swarm Optimisation algorithm was employed for hyperparameter selection. The hyperparameter-optimised model achieved a mean squared error of 0.00183 and an R^2 score of 0.979 during training, and a mean squared error of 0.00709 and an R^2 score of 0.887 during testing. Although the small discrepancy between training and testing metrics suggests slight overfitting, likely due to the size of the dataset, the model achieved a mean absolute percentage error of less than 10% during testing. Subsequently, process plots generated by the model predictions were used to identify suitable parameters, and a processing map was developed to highlight the window that achieves suitable dilution (14–24%), defect-free sound bonding, and thick and dense clads.

Keywords: artificial neural network; laser metal deposition; TiC/Ti6Al4V; process optimisation; cladding geometry

Academic Editor: Zhengyi Jiang

Received: 14 November 2025
Revised: 16 December 2025
Accepted: 20 December 2025
Published: 24 February 2026

1. Introduction

Additive manufacturing (AM) technology is a rapidly evolving field, offering numerous advantages over traditional subtractive manufacturing, including the flexibility to create intricate geometries [1,2]. Laser metal deposition (LMD) is one of the AM technologies that has attracted attention in the industry due to its versatility; the ability to create dense parts with good metallurgical bonding, higher degrees of freedom, scalability to fabricate more significant parts, and can be utilised to repair and weld structural parts [3,4]. LMD applications, such as coating and prototyping, require layer-by-layer building, which is achieved through the successive deposition of overlapping layers composed of side-by-side, overlapping single tracks [5]. These single tracks fundamentally serve as basic forming units of LMD process applications; their inherent properties, such as profile, dimensions and metallurgical consistency, directly influence both the overall cladding quality and process productivity [6–8].

Dense, thick, well-bonded, and crack-free layers are desired in cladding [6]. To achieve this, the geometric characteristics of the individual tracks need to be optimised [6]. Geometric characteristics of single tracks are often characterised by the clad height, width, and dilution. Dilution is a key factor in cladding, indicating how much of the feedstock and base material metal mix together [9]. Large dilution is associated with significant melt temperatures, which may lead to undesired excessive remelting of the prior layer and epitaxial growth [9]. Large dilution is an indication of unnecessarily high fraction of the laser's energy being used to melt the prior layer instead of being consumed by the deposited powders [7]. Clad height refers to the vertical buildup of consolidated powders above the substrate surface, while clad width represents the lateral spreading of the consolidated powders. Together, these geometric characteristics serve as important indicators of deposition quality and productivity [7]. Wider clads increase surface coverage per single pass, whereas the thicker heights reduce the number of layers required, thereby reducing the number of passes made during deposition [10,11]. Hence, thicker and denser clads, with minimal dilution, are desired.

The operating windows for the LMD process, in terms of geometric characteristics, are typically defined by three key processing parameters, including the laser power, scan speed, and powder feed rate [9,12]. Several studies [6,8,9,13,14] have investigated the influence of these processing parameters on geometric characteristics. It is reported that the thicker clads with minimal dilution are achieved with enhanced volume deposition, as the increase in powder feed rate leads to increased clad height, while dilution is progressively reduced [6–8,14]. However, the powder feed rate is reported to have a weak influence on clad width; it mainly contributes towards the vertical build of the clad [6]. The increase in scan speed leads to reduced clad height, width, and dilution [7,8,13]. The scan speed directly influences the volume of material deposited per unit time and the incident energy density [13]. Increasing the laser power was found to increase dilution and clad width, while exhibiting a negligible effect on clad height [6,14]. A controlled balance of these processing parameters must be achieved to fulfil the desired cladding quality.

The addition of ceramics such as TiC in Ti6Al4V alloy, resulting in the formation of a titanium metal matrix composite (TMMC), has been shown to suppress epitaxial growth while enhancing mechanical properties effectively [13,15,16]. However, undissolved TiC particles, which may retain inherent defects originating from powder production processes, can compromise tensile properties [17]. Accordingly, the operating window should promote sufficient dissolution and uniform dispersion of TiC phases to achieve a homogeneous microstructure and improved prospects of isotropic strengthening. While the amount of ceramic particles and their degree of dissolution are detrimental parameters for microstructural and mechanical properties of TMMCs, the addition of ceramics is often not considered to influence geometric characteristics by similar studies [18].

The complex physical phenomena associated with the process, coupled with the numerous processing parameters and evolving material states, complicate the development of an accurate predictive model and make optimisation challenging [19]. Various studies have proposed different modelling approaches to establish geometric and material properties of deposited tracks, including numerical models coupling heat and mass transfer [13,20,21], traditional statistical models [1,6,9,12,14,22], and artificial neural network (ANN) models [1,22]. Numerical models are often made with simplifying assumptions, such as material homogeneity and uniformity, to reduce computational demands and solve the problem within the available resources [13,20]. The challenge is accurately representing the melt pool dynamics, such as Marangoni and buoyancy effects, which significantly influence clad geometry [23]. Traditional statistical methods, such as the response surface method (RSM), are based on multivariable mathematical formulae that relate individual geometric charac-

teristics to process parameters [22]. Some studies [1,22] have shown that RSM, which relies on polynomial formulations, can be outperformed by ANNs when both are exposed to the same dataset. Unlike RSM, ANNs offer the advantage of modelling complex relationships directly from the data, without relying on explicit assumptions, predefined mathematical expressions, or prior knowledge of underlying trends. The objective of this study is to establish a range of processing parameters that yield optimal geometric characteristics by developing a processing map. This requires iterating through different process parameter combinations to generate prediction data. The choice of an appropriate modelling method is therefore guided by the need to (1) balance accuracy and computational time, (2) ease of incorporation and utilisation, (3) model only necessary properties independently while omitting additional interdependent factors that are not required for the objective at hand, and (4) consolidate all parameters into one model. Accordingly, ANNs provide the desired level of fidelity for the intended optimisation objective. Once trained, it can instantly generate data for the process map.

In this work, TiC/Ti6Al4V single tracks were fabricated via LMD, under varying processing parameters, i.e., laser power, scan speed, powder feed rate, and TiC content. The geometric characteristics of the produced clads were measured and recorded. Within the reviewed literature, no studies were identified that explicitly report on the influence of ceramic additions on clad geometric characteristics. Accordingly, a sensitivity study was conducted to assess the effect of TiC content on prediction accuracy using two model configurations: one that included TiC content as an input variable and the other that excluded it. Following this, an ANN model was developed to predict the clad geometric characteristics based on processing parameters, i.e., laser power, scan speed, and powder feed rate. The TiC content was consolidated with the Ti6Al4V content to determine the overall powder flow rate and was not considered as a separate factor for geometry predictions. A validated ANN model was used to generate prediction data, from which a process map was constructed. Examination of experimental samples revealed a suitable processing window within the processing map that achieves optimal geometric characteristics.

2. Materials and Methods

2.1. Materials

The powder materials used in the study were TiC and Ti6Al4V, with particle size distributions of 45–100 μm and 45–150 μm, respectively. SEM micrographs of the powders are presented in Figure 1. The TiC powder (Nanografi Nano Technology, Ankara, Turkey) shown in Figure 1a, exhibits coarse, irregular shapes. The Ti6Al4V powder (ECKART TLS GmbH, Bitterfeld, Germany), is distinguished by sphericity, as shown in Figure 1b.

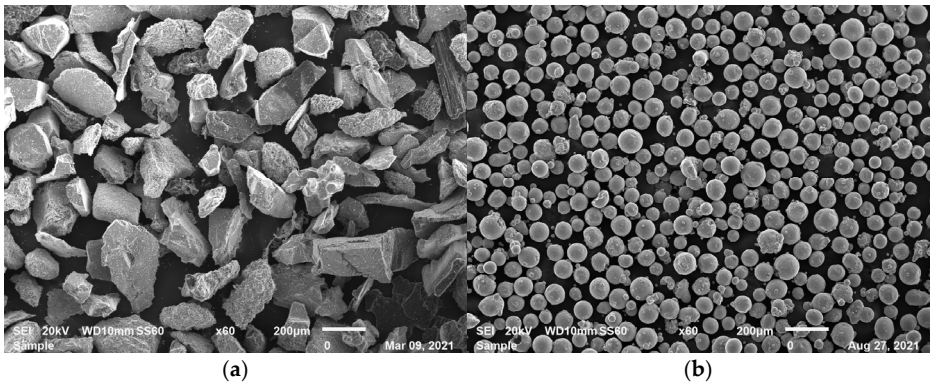

(**a**) (**b**)

Figure 1. SEM micrographs: (**a**) TiC; (**b**) Ti6Al4V.

2.2. Experimental Setup

A schematic of the deposition process is shown in Figure 2a. Single tracks, each 50 mm in length, were produced using a 3 kW Ytterbium fibre laser (manufactured by IPG Photonics, Marlborough, MA, USA), a 3-way continuous coaxial nozzle system, and a powder feeder system (manufactured by GTV, Luckenbach, Germany) integrated on a 6-axis robot (made by KUKA, Augsburg, Germany) for movement. The GTV powder feeder system comprised two feed hoppers, one containing Ti6Al4V and the other TiC. Argon (Ar) was used as the carrier gas for the powders at a fixed flow rate of 1.5 L/min. The powders were simultaneously delivered to a melt pool created on a sandblasted 6 mm thick Ti6Al4V substrate plate. During the deposition, the melt pool was protected from oxidation by Ar supplied at a fixed flow rate of 15 L/min. The laser beam diameter was fixed at 2 mm. The reviewed literature identifies laser power, scan speed, and powder feed rate as the key processing parameters governing the geometry of single tracks; accordingly, these variables were selected for systematic investigation. However, no studies were identified that determine the effect of ceramic content on cladding geometry. Effectively, the experimental design consisted of a mixed-level full factorial structure in which the laser power (1000, 1250, 1500 W) and scan speed (500, 1000 mm/min) were varied independently, while powder feed rate and TiC content were implemented as a coupled factor; each TiC concentration was intrinsically linked to a specific powder feed rate. The powder feed rate values are a consolidation of the Ti6Al4V and TiC mass flow rates. Due to the strong correlation between powder feed rate and TiC content, the influence of TiC on cladding geometry cannot be directly quantified. Instead, a sensitivity study was conducted to evaluate the effect of this parameter on prediction accuracy, presented later herein. This approach enables a robust investigation of key processing parameters without the need for extensive experimental runs. A total of 23 single-track specimens were produced, as presented in Table 1.

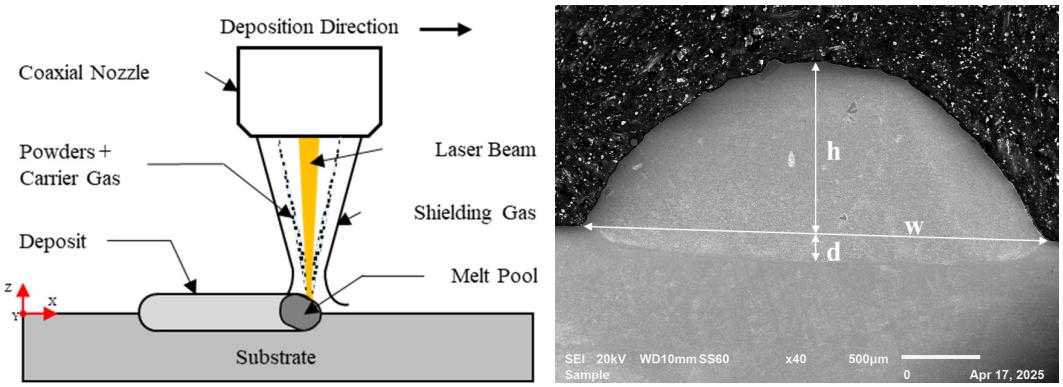

(**a**) (**b**)

Figure 2. Experimental Methods: (**a**) schematic of the LMD process; (**b**) single track cross-section.

Table 1. Process parameters and corresponding geometric characteristics.

Sample No.	Laser Power (W)	Scan Speed (mm/min)	Powder Feed Rate (g/min)	TiC Content (wt.%)	Height (mm)	Width (mm)	Depth (mm)	Dilution
1	1500	1000	7	5.3	0.687	3.056	0.302	0.305
2	1500	500	0.9	42.6	0.192	3.350	0.470	0.710
3	1250	500	5.3	14.6	1.121	2.911	0.198	0.150

Table 1. *Cont.*

Sample No.	Laser Power (W)	Scan Speed (mm/min)	Powder Feed Rate (g/min)	TiC Content (wt.%)	Height (mm)	Width (mm)	Depth (mm)	Dilution
4	1000	1000	3.1	24.8	0.360	2.438	0.196	0.353
5	1500	1000	3.1	24.8	0.394	3.119	0.359	0.476
6	1500	500	5.3	14.6	1.005	3.684	0.312	0.237
7	1000	500	7	5.3	1.336	2.695	0.110	0.076
8	1250	1000	5.3	14.6	0.565	2.743	0.207	0.269
9	1000	500	5.3	14.6	1.018	2.682	0.161	0.137
10	1500	500	1	50.1	0.224	3.308	0.470	0.678
11	1500	500	7	5.3	1.132	3.606	0.284	0.201
12	1250	1000	3.1	24.8	0.413	2.791	0.325	0.440
13	1000	500	3.1	24.8	0.696	2.700	0.278	0.286
14	1000	1000	7	5.3	0.818	2.245	0.179	0.180
15	1250	500	7	5.3	1.313	3.231	0.197	0.131
16	1000	1000	5.3	14.6	0.521	2.373	0.134	0.205
17	1250	500	3.1	24.8	0.684	3.164	0.301	0.306
18	1500	1000	5.3	14.6	0.549	3.195	0.325	0.372
19	1500	500	1.3	60.7	0.261	3.220	0.520	0.666
20	1500	500	1.1	55.7	0.249	3.212	0.500	0.667
21	1500	500	3.1	24.8	0.567	3.786	0.524	0.480
22	1500	500	1.7	45.1	0.336	3.153	0.505	0.600
23	1250	1000	7	5.3	0.665	2.708	0.243	0.267

2.3. Sample Preparation

Produced single tracks were sectioned perpendicular to the deposition direction using the Brilliant 200 cut-off machine (by ATM, Mammelzen, Germany). The prepared samples were mounted using the CitoPress-15 automatic press (Struers, Ballerup, Denmark) with Struers MultiFast Bakelite resin with wood filler (supplied by Advanced Laboratory Solutions, Randburg, South Africa). Thereafter, the samples were mechanically ground using the SAPHIR 550 grinding and polishing machine (by ATM, Mammelzen, Germany) with silicon carbide papers of grit sizes 80, 320, 1200, and 4000. Ground samples were polished to a high-gloss finish using Struers Diapro MD-mol 3 µm diamond suspension (supplied by Advanced Laboratory Solutions, Randburg, South Africa), followed by a 3-min final polish with colloidal silica 0.04 µm OP-S suspension. The samples were etched using Kroll's reagent, a mixture containing 100 mL of water, 1–3 mL HF, and 2–6 mL HNO_3, in accordance with ASTM E407-07 [24]. Macrostructures and microstructures were analysed using a JEOL JSM-6010PLUS/LA scanning electron microscope (SEM) (manufactured by JEOL Ltd., Tokyo, Japan). Subsequently, the geometric characteristics, width (w), height (h), and depth (d), were measured from SEM micrographs using ImageJ software (version 1.54g), as illustrated in Figure 2b. The ImageJ software package is used in various materials science investigations [13,17,25]; the measurements are given in Table 1. Dilution (D) was calculated as follows [6,9].

$$D = \frac{d}{d + h} \quad (1)$$

2.4. Artificial Neural Network

An ANN model consisting of a single hidden layer was implemented using the Keras library within the TensorFlow framework. The three-layer architecture has been successfully used in other studies [1,2,22]. The network architecture is illustrated in Figure 3. The input layer consists of neurons representing processing parameters. Based on established findings that laser power, scan speed and powder feed rate influence clad geometry,

these parameters were selected as input variables for the model. The impact of TiC on geometry has not been established in the existing literature. Since the powder feed rate and TiC content were coupled, the direct influence of TiC on cladding geometry cannot be independently quantified. Consequently, a sensitivity study will be performed later to evaluate how this parameter influences prediction accuracy, informing whether it should be included within the model development framework. The output layer comprises neurons representing geometric properties.

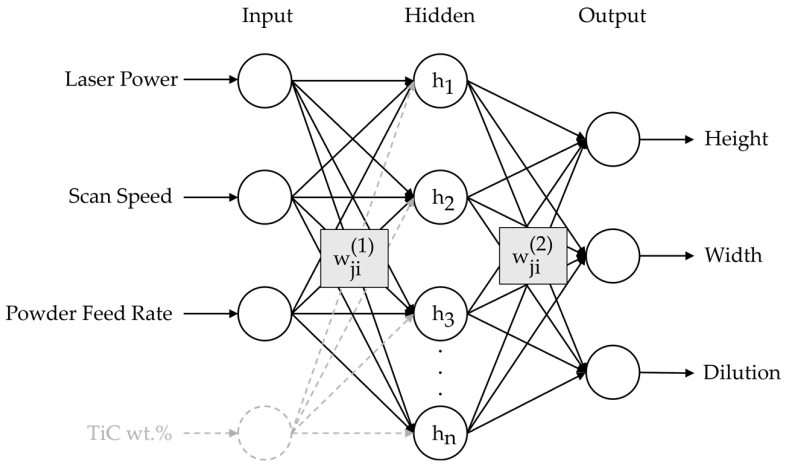

Figure 3. Schematic of an ANN.

The number of neurons in the hidden layer is determined using an empirical formula [22,26]

$$h = \sqrt{p + q} + a \tag{2}$$

where h is the number of hidden neurons, p is the number of input neurons, q is the number of output neurons, and a is an integer ranging from 1 to 10. The exact number of hidden neurons will later be determined using the Particle Swarm Optimisation algorithm. The lines connecting neurons represent weighted signals, where the weights determine the strength of influence each neuron has on the next. The input, hidden, and output layers are denoted by indices L = 0, L = 1, and L = 2, respectively. The weight matrix $w_{ji}^{(1)}$ corresponds to the weights associated with signals transmitted from the input layer to the hidden layer, while $w_{ji}^{(2)}$ represents the weights regulating signal transmission from the hidden layer to the output layer. The elements of these matrices represent the weight values associated with signals transmitted from the ith neuron of layer $(L - 1)$ to the jth neuron of layer (L).

The input layer introduces the process parameters into the network, while the output layer generates predictions of geometric characteristics. The hidden layer serves as an intermediate computational stage, facilitating the transfer of information between the input and output layers. It is responsible for processing and transforming input signals, which are then transferred to the output layer and transformed into final predictive outputs. A hyperbolic tangent activation function was employed in the hidden layer. This function has been demonstrated by Song et al. [1] to be effective in modelling the clad height and width of 316 L stainless steel, which is expressed as follows:

$$g(u^{(1)}) = \frac{1 - e^{u^{(1)}}}{1 + e^{u^{(1)}}} \tag{3}$$

where $u^{(1)}$ is a vector whose elements denote the weighted input signals in the hidden layer, which can be determined using the expression

$$u^{(L)} = w_{ji}^{(L)} \cdot x_i^{(L-1)} + b_j^{(L)}, \quad (4)$$

where $u^{(L)}$ denotes a vector of weighted input signals of the layer (L), $x_i^{(L-1)}$ is a vector of signals from layer (L − 1), $w_{ji}^{(L)}$ is the weight matrix for signals transmitted into layer (L), and $b_j^{(L)}$ is the corresponding bias vector for layer (L). A linear activation function was utilised in the output layer to enable the model to extrapolate over the entire real number range $(-\infty, \infty)$, beyond the training data range of [0, 1], and is expressed as

$$f(u^{(2)}) = u^{(2)} \quad (5)$$

The error metrics used in the study are the mean squared error (MSE) and R^2 score. The MSE was used as a loss function, whereas the R^2 score was employed to measure the model fitting. The Adam optimiser was used for updating weights and biases.

2.5. Data Handling

Out of the 23 experimental samples presented in Table 1, 15 samples were used for training, 4 for validation, and 4 for testing. The data is distributed over different orders of magnitude, and normalisation was applied to prevent variables with larger values from dominating the learning process. Normalisation was applied based on the training dataset, using the following equation.

$$X_{norm} = \frac{X - X_{max}}{X_{max} - X_{min}} \quad (6)$$

Here, X_{norm} is the normalised value, X is the original value, X_{min} and X_{max} are the minimum and maximum values of the corresponding variable observed in the training dataset, respectively. As a result, only training data is constrained to the [0, 1] range. Since the normalisation parameters (X_{min} and X_{max}) are derived solely from the training set, the normalised validation and test datasets may contain values outside this range.

2.6. Hyperparameter Selection and K-Fold Validation

Hyperparameter optimisation entails the selection or fine-tuning of the neural network's parameters to maximise its performance [2]. This is achieved by exploring various hyperparameter configurations. In this study, the number of neurons (h) in the hidden layer and exponential decay rates (β_1 and β_2) of moment estimates of the Adam optimiser were selected using the particle swarm optimisation (PSO) algorithm. PSO was first proposed by Kennedy and Eberhart [27] in 1995. It belongs to a class of bio-inspired algorithms as it mimics the cooperative behaviour of a flock of birds and a school of fish. The algorithm utilises a population of particles that individually navigate a defined multidimensional domain. The movements of each particle are guided by the best position ever known locally by the particle and the best-realised position globally. The algorithm was implemented using the PySwarms library licensed by MIT [28]. The inertia coefficient was set to 0.5, and the acceleration coefficients were both set to 2; these parameters were successfully used by Pant and Chatterjee [26]. Three particles were used for five iterations.

A small dataset poses the risk of overfitting and poor generalisation [2]. K-fold cross-validation is a method used to evaluate a model's ability to generalise well to unseen data [2]. It is particularly useful for preventing overfitting in small datasets. The technique involves dividing the original dataset into k subsets, and the model is trained on k − 1 subsets

while the remaining subset is used to evaluate the model's performance. This process is repeated k times, with each subset used as an evaluation subset once. Early stopping was implemented to terminate training once the validation loss converged, thereby preventing overfitting and saving time.

3. Results and Discussion

3.1. Effect of TiC Content on ANN Prediction Accuracy

The inherent correlation between the powder feed rate and TiC content renders the application of feature importance algorithms ineffective for quantifying or assessing the effect of TiC content as an independent variable on geometric characteristics. Nevertheless, a sensitivity study comparing model performance with and without the inclusion of TiC can be conducted to evaluate its overall impact on model performance. Accordingly, the influence of TiC content (wt.%) as an input parameter on the prediction of geometric characteristics was investigated by developing two sets of models: one that included TiC content as an input parameter and another that excluded it.

For each case, model performance was evaluated across different network architectures by varying the number of neurons in the hidden layer from 3 to 14, encompassing both models as determined by Equation (2). All the models were trained with the default Adam optimiser hyperparameters (learning rate of 0.001, β_1 = 0.9, and β_2 = 0.999), and early stopping was implemented to mitigate overfitting. The predictions were made for samples 20 through 23 in Table 1, corresponding to TiC contents of up to 55.7 wt.%. The prediction performance of the models, quantified in terms of mean absolute percentage error (MAPE) for height, width, and dilution, is presented in Figure 4. The line plots display the variation in MAPE with the number of hidden neurons, while the bar plots illustrate the difference in MAPE between the two model configurations.

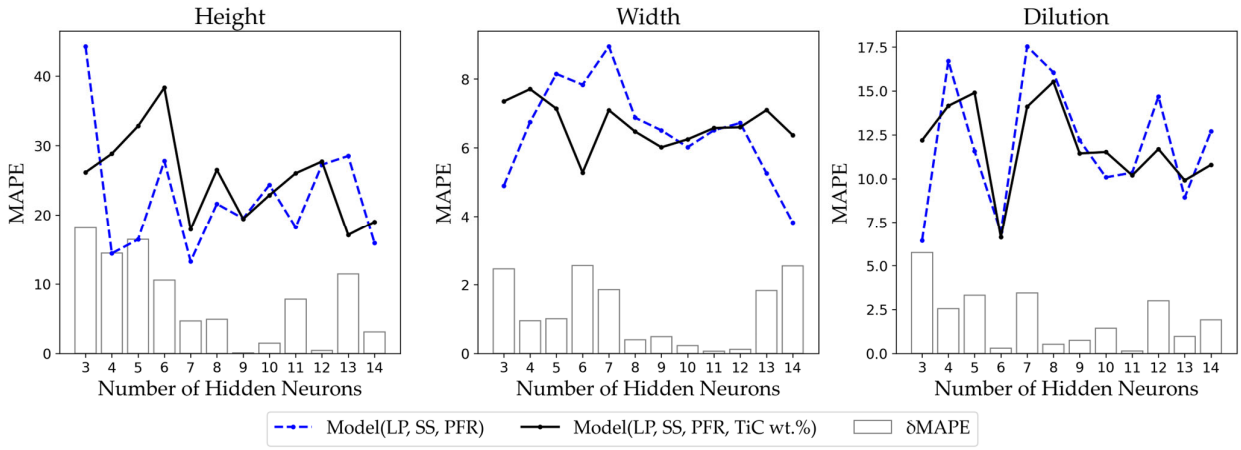

Figure 4. Comparison of ANN prediction performance (MAPE) for geometric characteristics with and without TiC content as an input parameter.

The results indicate that variations in network architecture resulted in only marginal differences in predictive performance between the models. Notably, the model excluding the TiC content as an input parameter consistently achieved the lowest overall MAPE for each geometric characteristic. Furthermore, the differences in MAPEs between the two model configurations were relatively small, particularly for width and dilution predictions, with a δMAPE of less than 6%. For height prediction, larger discrepancies in MAPE were observed at lower hidden neuron counts. As the number of neurons increased, the difference in prediction error between the models decreased.

These findings suggest that including TiC content as an input variable does not result in a significant improvement in model performance. Accordingly, the comparable performance observed between models with and without TiC content should be interpreted as guidance for the input parameter selection rather than as evidence regarding the intrinsic influence of TiC content on geometric properties, given that variations in TiC content were coupled with powder feed rate in this study. In light of the similarity in predictive accuracies, TiC content was excluded from subsequent model development. This decision simplifies the modelling and optimisation framework by reducing the number of control variables without compromising prediction accuracy.

3.2. Hyperparameter Selection and K-Fold Cross Validation

Hyperparameter selection was conducted for the model configuration of three inputs, i.e., the laser power, scan speed, and powder feed rate, illustrated in Figure 5. After five iterations of the PSO algorithm, a minimum MSE was achieved with a configuration consisting of eight hidden neurons, h, β_1 set to 0.64, and β_2 set to 0.67.

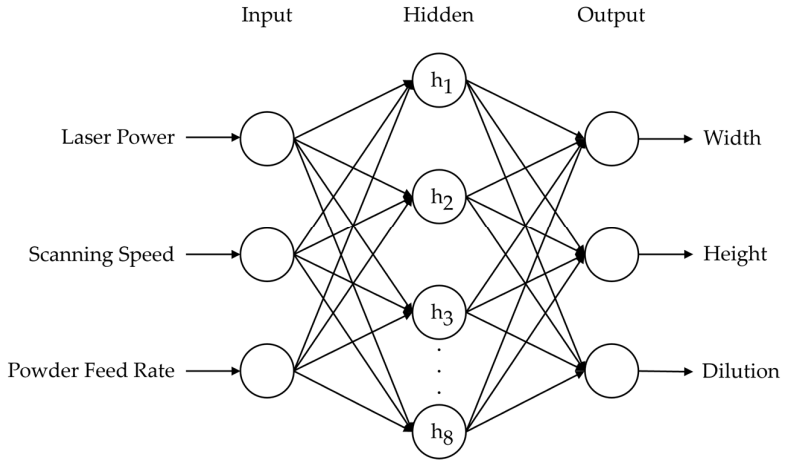

Figure 5. Schematic of the Implemented ANN architecture.

This configuration was cross-validated using K-Fold. Figure 6 presents the cross-validation histories of the model. Figure 6a shows that the model slightly overfitted the third fold, as the MSE validation curve is visibly higher than the training curve. The other three folds have an acceptable fit. The average MSE for the folds was determined to be 0.0050. Similar observations are made in the R^2 score curves, shown in Figure 6b. The average cross-validation R^2 score was 0.919. The aggregated metrics suggest that the model performs well. Therefore, the model is considered suitable for prediction and optimisation purposes.

The cross-validated model was trained for the last time to preserve the learnable parameters. Figure 7 shows the learning history of the model. Training and validation curves maintained a small, consistent gap, indicating that the model was learning and generalising effectively. The MSE declined as the model iterated, indicating that it was learning. Early stopping was implemented once convergence was reached. Figure 8 shows the best-fit plots of model predictions made from training data at the end of training. The model achieved an MSE of 0.00183 and an R^2 score of 0.979.

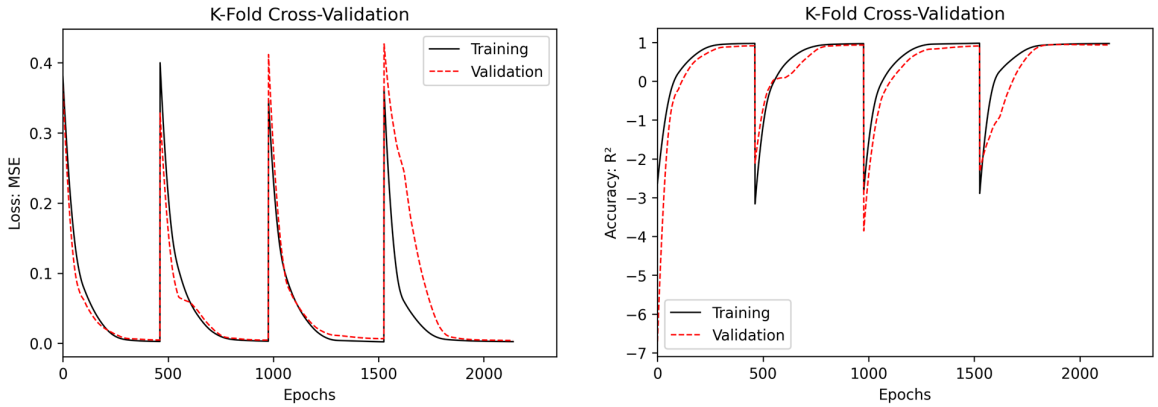

(**a**) (**b**)

Figure 6. 4-Fold cross-validation histories (**a**) MSE Loss, (**b**) R^2 score.

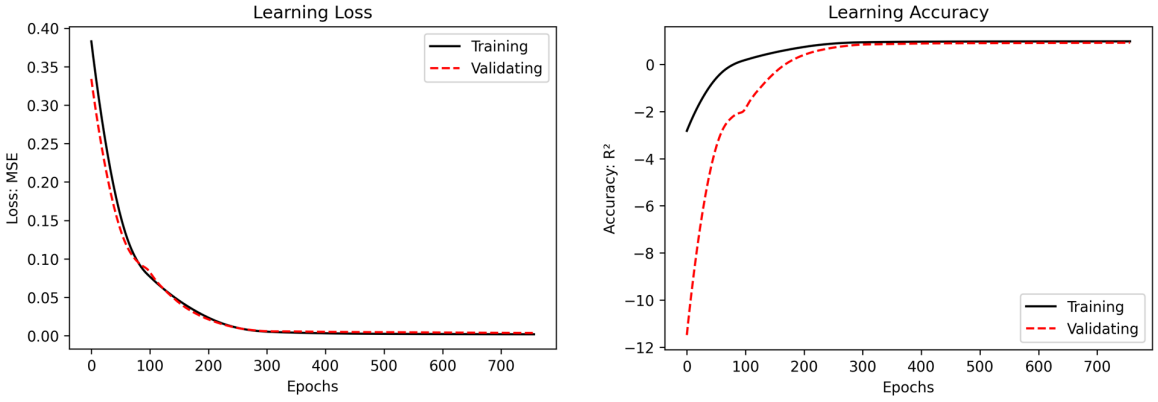

(**a**) (**b**)

Figure 7. Model training history: (**a**) MSE vs. Epochs; (**b**) R^2 score vs. Epochs.

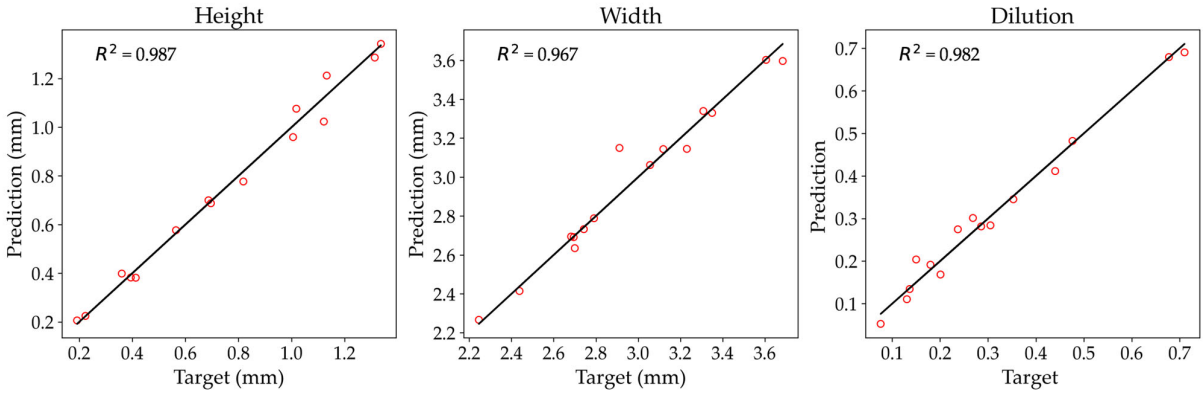

Figure 8. Best fit plots at the end of training.

3.3. ANN Model Testing

Four previously unseen experimental samples, samples 20 to 24 in Table 1, which were not introduced at any stage of the training or validation processes, were used to evaluate the model's predictive accuracy. Table 2 presents a summary of the results. Here, h denotes the measured height, $\hat{h}$ represents the predicted height, and δh indicates the absolute percentage error. This nomenclature is similarly applied to width (w) and dilution (D). In the prediction of height, the maximum and mean absolute errors (MAE) were 9.99% and 5.77%, respectively. For width, the errors were 7.91% and 5.25%. For dilution, the errors were 11.48% and 4.11%. The MSE and R^2 scores are 0.00709 and 0.887, respectively.

Table 2. Comparison of ANN model predictions and experimental observations.

Sample No.	h (mm)	$\hat{h}$ (mm)	δh (%)	w (mm)	$\hat{w}$ (mm)	δw (%)	D	$\hat{D}$	δD (%)
20	0.249	0.243	2.74	3.212	3.349	4.24	0.667	0.668	0.18
21	0.567	0.600	5.61	3.786	3.508	7.36	0.480	0.460	4.28
22	0.336	0.352	4.73	3.153	3.403	7.91	0.600	0.603	0.48
24	0.665	0.732	9.99	2.708	2.668	1.48	0.267	0.237	11.48

The results obtained are consistent with those reported in similar studies. Song et al. [1], employing a similarly small dataset of 20 samples, achieved average errors of 4.39% and 2.79% in predicting clad width with an RSM and ANN model, respectively. For height prediction, they achieved an average error of 7.52% and 0.18%. Nezhad et al. [25] utilised the RMS technique to predict cladding width, height, wetting angle, penetration depth, and dilution, achieving reported average errors of 3.40%, 2.48%, 4.41%, 7.61%, and 8.55%, respectively. The disparity between testing and training metrics in the current study implies a slight overfitting. Nonetheless, the model achieved an aggregated MAE greater than 90% on the testing data, suggesting it can be potentially deployed for predictive applications and for developing a process map.

3.4. Interaction of Process Parameters

To develop a process map and identify suitable process parameters, it was first important to determine the impact of process parameters on geometric characteristics. As established from the literature [1,6], the level of influence each process parameter has is contingent upon the specific settings of other process parameters. Hence, it was more effective to visualise these interactions through 3D surface plots. This facilitates a comprehensive understanding of the process behaviour and supports more informed optimisation efforts. Only three process parameters are considered in this study, i.e., laser power, scan speed, and the powder feed rate. The interactions between a pair of process parameters were investigated by fixing the third parameter. Literature indicates that the combination of high powder feed rates and scan speeds, with lower laser power, leads to poor metallurgical bonding, and the deposited material detaches from the substrate [6,18]. In contrast, low powder feed rate and high laser power produce a deep melt pool, risking excessive remelting of substrate material [6,18]. To establish a balance between these competing effects, interaction curves were derived using a high laser power (1500 W), high powder feed rate (7 g/min) and a low scan speed (500 mm/min).

3.4.1. Effect of Process Parameters on Width

Figure 9 presents the effects of processing parameters on width. Figure 9a shows the interaction of laser power (*LP*) and scan speed (*SS*), at a fixed powder feed rate (*PFR*). With increasing *LP*, the melt pool width expands, while increasing *SS* leads to its reduction. This observation agrees with reported work [1,6]. Increasing the *LP* leads to greater heat energy accumulation within the melt pool, thereby raising the overall temperature levels [20], and the material is melted. Increasing the *SS* shortens the interaction time between the laser beam and the material, reducing the accumulation of heat energy [13].

According to Figure 9b, *PFR* has a minor influence on melt pool width, while the *LP* consistently demonstrates a strong positive correlation with width across all *PFR* levels. This is in agreement with reported works [1,7,25]. Raising the *PFR* supplies additional material to the melt pool, and increasing *LP* increases heat accumulation, thereby facilitating the formation of wider clads.

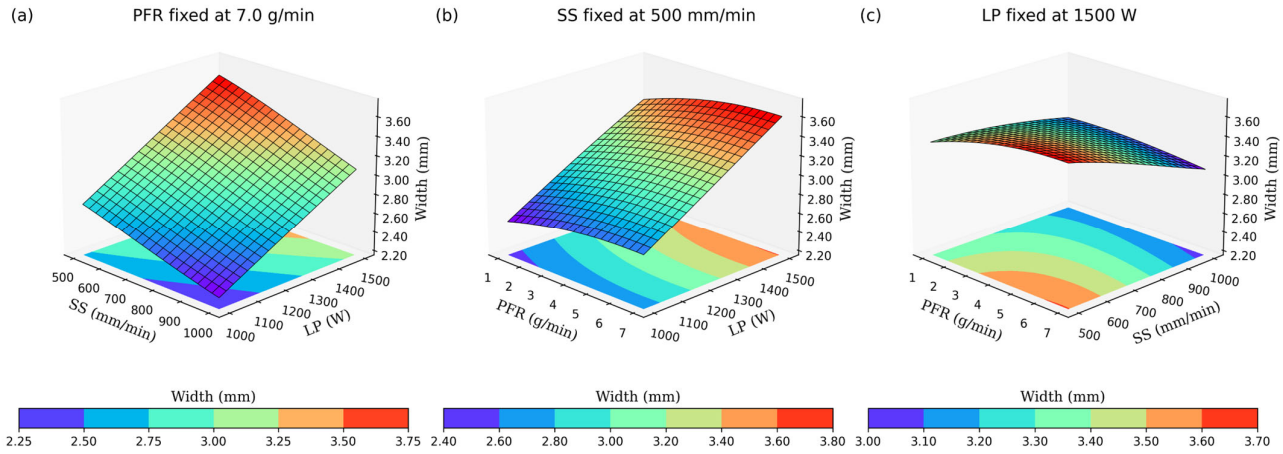

Figure 9. Interaction of process parameters on width: (**a**) LP and SS; (**b**) LP and PFR; and (**c**) SS and PFR.

Figure 9c shows the *SS* and *PFR* interaction at constant *LP*. The width decreases as the *SS* increases and the *PFR* decreases. Over the processing window being investigated, the melt pool width is mainly regulated by *LP*, followed by *SS*. The *PFR* has the least effect on the width.

3.4.2. Effect of Process Parameters on Dilution

Figure 10 presents the interaction of process parameters on dilution. Figure 10a illustrates the interaction of *LP* and *SS* at a fixed *PFR*. An increase in *SS* and *LP* leads to greater dilution. Melt pool growth is facilitated by Marangoni phenomena and conductive heat transfer at the liquid-solid interface [13,29]. The Marangoni phenomenon is the transfer of liquid from an area of low surface tension to an area of high surface tension [29]. Surface tension gradients are induced by temperature gradients within the melt pool [6,29]. The hotter liquid directly underneath the heat source, with lower surface tension, is radially pulled outwards from the centre towards the edges by the cooler liquid with higher surface tension [6]. Through conduction and convection, the liquid metal drops in temperature and then returns to the centre, and the cycle repeats. As the heat sinks into the substrate, the melt pool grows [6]. Increasing the *LP* raises both the overall temperature and temperature gradients, which in turn enhance heat transfer into the substrate. As a result, a wider and deeper melt pool is formed. An increase in *SS* leads to reduced laser energy coupling into the material [20]. Concurrently, the mass of powder deposited per unit length decreases. Overall, this appears to have a positive impact on dilution, as the reduced powder flow into the substrate allows a proportion of the laser energy to interact with the substrate, thereby promoting deeper dilution. Comparable findings have been reported by Barekat et al. [6] and Liu et al. [9].

According to Figure 10b, dilution is minimised by increasing the *PFR*. As more mass is deposited per unit length, an increasing proportion of the laser energy goes into melting the powder particles instead of the substrate, leading to reduced penetration [6]. At a constant *LP*, the influence of *SS* on dilution is negligible across the range of *PFRs* investigated, as illustrated by Figure 10c. Dilution exhibits a greater sensitivity to the *PFR* than *LP*; minimal dilution can be achieved at high *PFRs*.

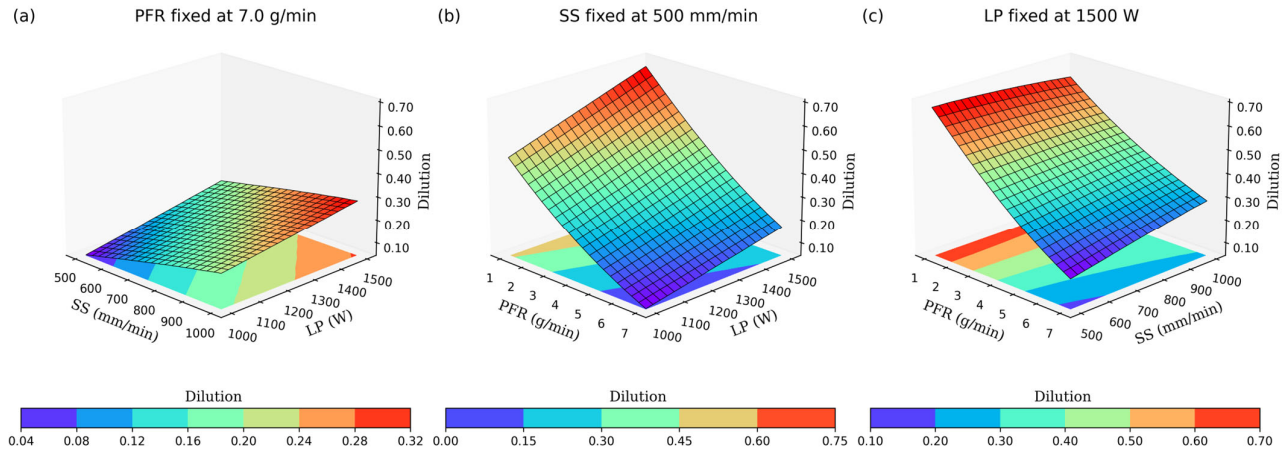

Figure 10. Interaction of process parameters on dilution: (**a**) LP and SS; (**b**) LP and PFR; and (**c**) SS and PFR.

3.4.3. Effect of Process Parameters on Height

Figure 11 presents the interaction between processing parameters and clad height. Figure 11a shows the combined effect of *SS* and *LP* at a fixed *PFR*. An increase in the *SS* leads to a reduction in clad height. The influence of *LP* on cladding height appears to be minimal, a trend consistent with the findings reported in previous studies [6,14,20]. Notably, greater clad thickness is observed under conditions of low *SS* and high *LP*. This can be attributed to a combined increase in the material feed into the melt pool and the higher energy input associated with increased *LP*, which facilitates a greater catchment efficiency by promoting the formation of a wider melt pool [7].

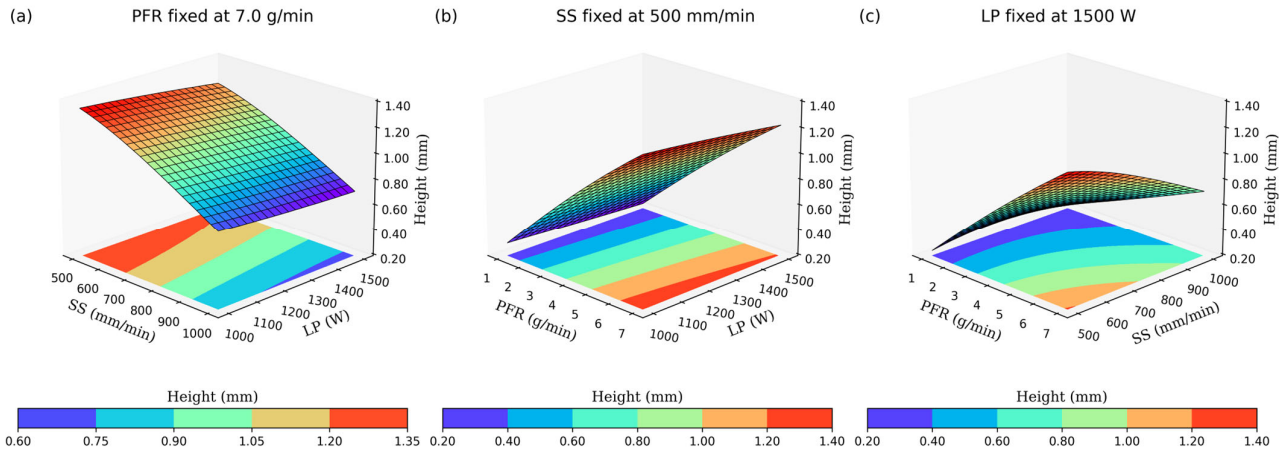

Figure 11. Interaction of process parameters on height: (**a**) LP and SS; (**b**) LP and PFR; and (**c**) SS and PFR.

Clad height exhibits a positive correlation with *PFR* in Figure 11b. At a fixed *LP*, the *PFR* is observed to have a greater influence on clad height compared to the *SS*, as shown in Figure 11c. While both parameters govern the volume of material delivered to the melt pool, the *PFR* plays a more significant role in the vertical buildup of the clad. The *SS* affects both the vertical buildup and lateral spreading of material by regulating the melt pool width, as exhibited in Figure 9. Enhanced input energy and material deposition lead to more prominent clads, characterised by greater heights and increased width.

3.5. Development of Processing Map

In the context of this study, the optimal processing window is defined primarily by achieving minimum dilution, followed by good metallurgical bonding, and the formation of thick and dense clads, in that order of priority. Dilution must be effectively controlled to prevent poor bonding or excessive remelting of the substrate. Additionally, the formation of dense and thick clads is essential for achieving good deposition efficiency. Reported suitable dilution levels vary across studies, largely due to differences in the materials being investigated. Barekat et al. [6] suggest a range between 10% and 20%, Fan and Zhang [14] report an optimal value of 6%, Dalaee et al. [7] indicate a range between 14% and 36%, while Erfanmanesh et al. [12] established a range between 30% and 45%. Based on these findings, the search for a suitable dilution window can be constrained to a range between 6% and 45%. According to the plots in Figure 10, with the *SS* fixed at 500 mm/min, this dilution range can be achieved for $PFR > 3$ g/min and $LP \geq 1000$ W.

Figure 12 presents the cross-sectional views of experimental samples fabricated at SS of 500 mm/min, categorised according to the *PFR* and *LP* applied. The samples are hereafter designated as TMMC1 through TMMC9. All samples exhibit good fusion, with no visible cracks. At each *LP* level, samples fabricated with a lower *PFR* setting generally exhibit deeper penetration depths, reduced clad heights, and increased clad widths. Whereas samples produced with the highest *PFR* setting exhibit shallower penetration depths, greater clad heights, and narrower widths. TMMC7 and TMMC8 exhibit asymmetric profiles and evidence of an emerging lack of fusion defect, attributed to excessive *PFR* in combination with insufficient *LP* [30]. Excessive powder flooding, coupled with inadequate laser energy input, led to the formation of narrow and vertically thick clads, which ultimately became unstable. In contrast, when the laser energy input is adequate, as with TMMC6 at 1500 W *LP*, enhanced penetration and lateral expansion of the melt pool facilitated effective spreading of the powders. Hence, TMMC6 exhibits a more favourable profile compared to TMMC4 and TMMC5. The interplay between *PFR* and *LP* during the cladding process can be quantitatively evaluated using the aspect ratio (AR), defined as the ratio of clad width to its height [7]. TMMC4 and TMMC5 exhibit AR values of 2.02 and 2.46, respectively.

Notably, samples fabricated with the highest TiC content display the largest undissolved particles. The quantity and dissolution degrees of TiC particles within the matrix have been reported to impact cladding quality [17]. Due to internal defects in powder particles, undissolved TiC particles compromise the tensile properties of composites [17,31]. Moreover, increasing TiC content has been shown to reduce elasticity [31]. Conversely, wear and hardness properties have been reported to positively correlate with both the presence of undissolved TiC particles and higher TiC content [13]. TMMC4, TMMC7, and TMMC8 exhibit rough surfaces with bumps, primarily due to unmolten particles and droplet spattering. Rough profiles have been reported to facilitate the entrapment of gas during the deposition of a new layer, causing the formation of pores [32].

Ideally, complete dissolution is preferred to retain a balance between ductility and enhanced strength. However, as the primary focus of this study is the optimisation of geometric characteristics based on dilution levels to maximise process efficiency, a larger fraction of the laser energy should be absorbed by the deposited powders. Samples TMMC1 through TMMC3 are excluded as suitable candidates due to their high dilution and lesser clad thickness, while TMMC7 and TMMC8 are eliminated due to displaying early signs of a developing lack of fusion and poor clad profiles. Consequently, TMMC4, TMMC5, TMMC6, and TMMC9, each exhibiting favourable clad profiles, were identified as suitable candidates for the effective deposition process. These samples demonstrated minimal dilution, along with thick and dense clads, and were therefore selected for further metallurgical analysis.

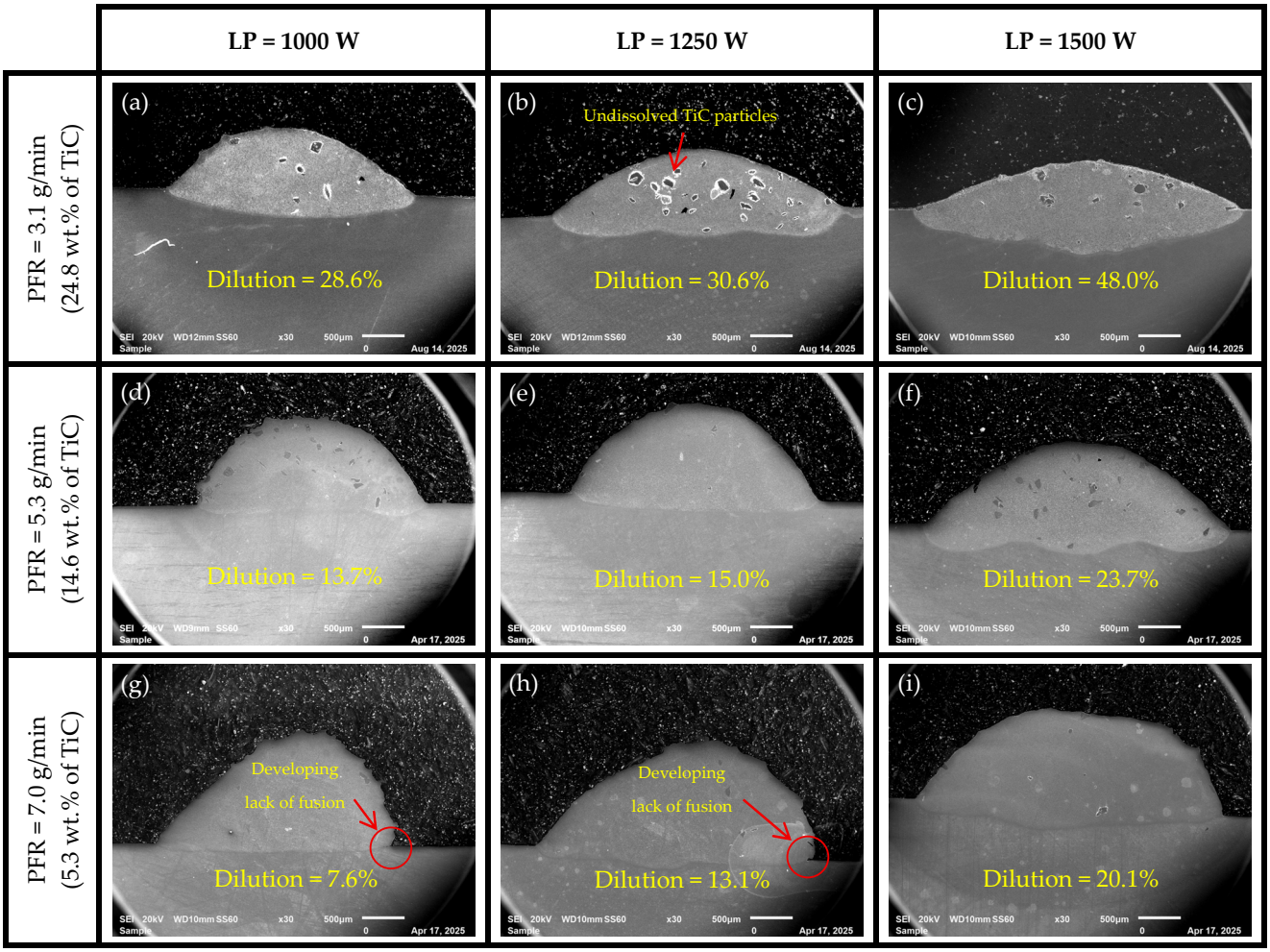

Figure 12. Cross-sections of deposited clads: (**a**) TMMC1, (**b**) TMMC2, and (**c**) TMMC3, (**d**)TMMC4, (**e**) TMMC5, (**f**) TMMC6, (**g**) TMMC7, (**h**) TMMC8, and (**i**) TMMC9.

SEM micrographs of the microstructures of the samples taken at the centre of the clads are presented in Figure 13. The samples exhibit no observable defects. Notably, TMMC4, TMMC5 and TMMC6 exhibit equiaxed prior β-Ti grains with distinguishable morphological characteristics of TiC phases. The observed TiC phases include chainlike structures forming at the grain boundaries, as well as equiaxed, dendritic, and granular TiC. By measuring the area fractions of the TiC over the Ti6Al4V matrix using ImageJ software, it was found that TiC phases in TMMC4 occupy approximately 10.3%, 21.1% in TMMC5, and 19.3% in TMMC6. Moreover, the size of the granular and equiaxed TiC phases in TMMC4 ranges between 2 and 6 µm, 2–10 µmin TMMC5, and 2–8 µm in TMMC6. This is attributed to the differences in their thermal histories, often represented by the G/R ratio, where G is the temperature gradient, and R is the solidification rate, which governs grain morphology [33]. Since the *SS* was fixed, the solidification rate R remained constant [13,33]. TMMC6 was fabricated at a higher *LP*, had a better catchment efficiency of the powder particles, resulting in a larger clad, and hence developed lower temperature gradients G than TMMC4 and TMMC5 [34]. Therefore, a lower G/R value led to the evolution of the dominant equiaxed dendritic TiC morphology. In contrast, the higher G/R value of TMMC5 led to the development of columnar dendritic TiC and coarser equiaxed TiC. TMMC6 exhibits columnar grains with uniformly dispersed rod-shaped TiC. The TiC content added has not promoted the growth of equiaxed grains. The columnar grains grew

upright to the bond zone towards the melt pool centre, in the direction of the temperature gradient [13].

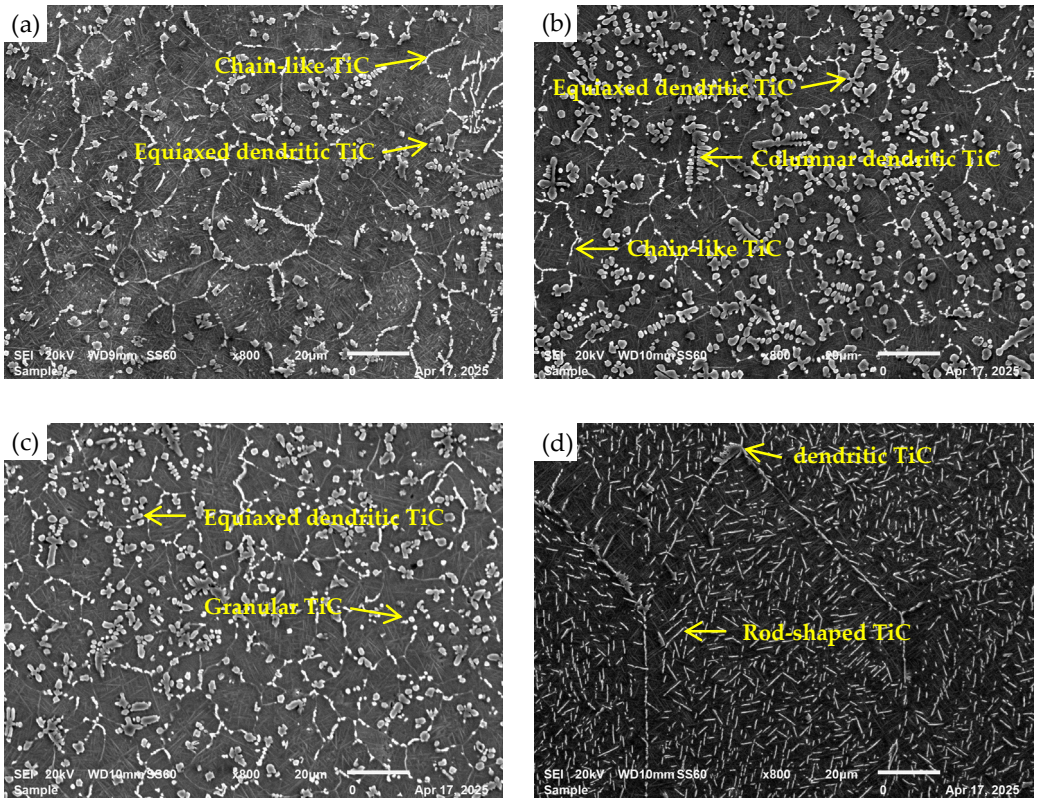

Figure 13. SEM Micrographs of: (**a**) TMMC4, (**b**) TMMC5, (**c**) TMMC6, and (**d**) TMMC9.

A process map was constructed for LMD of TiC/Ti6Al4V single tracks, within the studied experimental domain, shown in Figure 14. The map links clad geometric characteristics, i.e., dilution (D), width (w), and height (h), to process parameters. The observed processing window is based on TMMC4, TMMC5, TMMC6, and TMMC9; therefore, a suitable dilution falls between 14% and 24%. The hatched area indicates the processing window. Based on the results presented, this processing window achieves a decent degree of TiC dissolution while maintaining a satisfactory clad profile. TMMC7 and TMMC8 exhibited a developing lack of fusion defects, attributed to high powder feed rate and low to moderate laser power. These samples have aspect ratios of 2.0 and 2.5, respectively. Based on these observations, it is inferred that an AR of 2.5 or lower risks the development of a lack of fusion. The shaded area on the process map shows this region. In general, the process map can be used to select process parameters that attain the desired geometric characteristics.

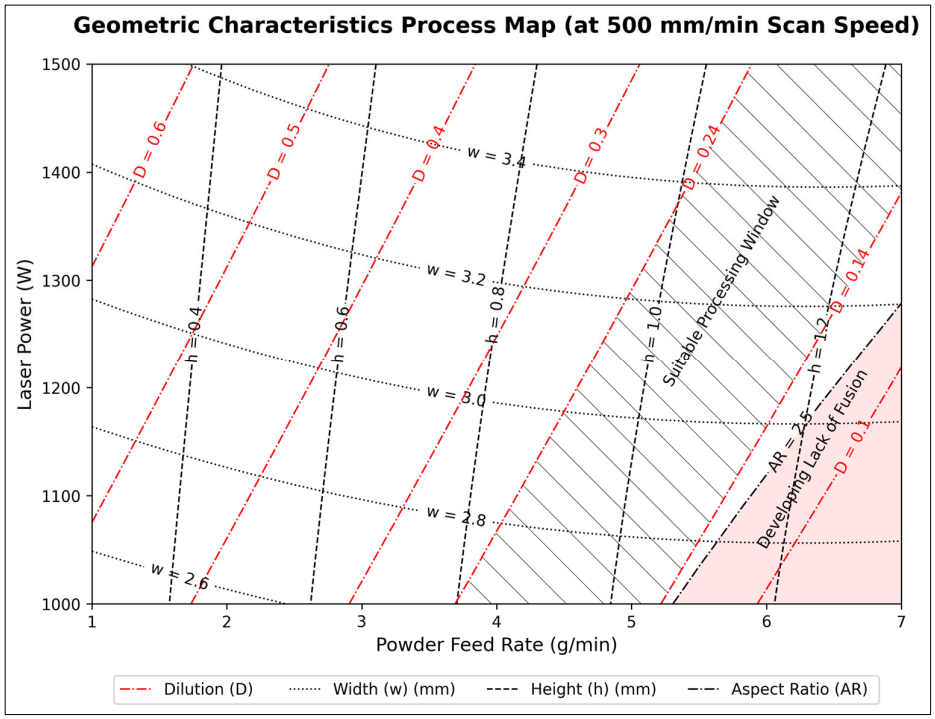

Figure 14. LMD process map for TiC/Ti6Al4V single tracks.

4. Conclusions

An optimal processing window to achieve minimal dilution, dense, and thick clads is established based on predictions made from a developed ANN model and metallurgical characterisation of TiC/Ti6Al4V experimental single tracks. The ANN model was developed to predict geometric characteristics, including clad width, height, and dilution. The developed model was found to achieve good prediction metrics, which are comparable to those reported in the literature for similar regression studies. In the test phase, the model achieved an MSE of 0.00719 and an R^2 score of 0.885, proving its effectiveness in producing accurate predictive data for process plots.

The combined effects of processing parameters on geometrical characteristics were investigated. It was found that clad height is primarily influenced by powder feed rate, followed by the scan speed, while the laser power has a negligible influence. Clad width is mainly influenced by laser power and scan speed. Dilution is predominantly influenced by the powder feed rate, with the scan speed and laser power exhibiting comparable levels of influence.

The understanding of combined interactions of process parameters and geometric characteristics, coupled with metallurgical examination of experimental samples, supported optimisation efforts. A suitable operating window for achieving adequate dilution while producing thicker and denser clads with no observable defects was identified at a low scan speed of 500 mm/min, combined with a high powder feed rate (approximately 3.7 to 7 g/min) and laser power (1000 to 1500 W).

The addition of TiC particles led to the formation of in situ TiC particles exhibiting distinct morphologies under varying processing conditions. Undissolved TiC were more prominent in samples with higher TiC content. Increasing the laser power enhanced the dissolution of TiC particles, as evidenced by the increased area fraction of in situ TiC phases within the matrix. Moreover, samples containing 14.6 wt.% TiC exhibited equiaxed grains, in contrast to the 5.3 wt.% TiC sample, which exhibited columnar grain structures.

ANN algorithms are useful for process-property modelling and optimisation. However, the quality and quantity of the training data influence model accuracy and robustness. For future work, the dataset should be expanded and diversified to enhance model robustness. Moreover, to investigate the implications of the processing window beyond single tracks, horizontal layers and cubic samples should be produced. The constructed processing map, once validated by horizontal and cubic samples, could potentially reduce experimental trials, improve process productivity, and significantly reduce costs for cladding applications. In addition, the mechanical properties directly influenced by the addition of TiC should be investigated, enabling optimisation of the TiC content.

Author Contributions: Conceptualisation, T.T., B.M. and P.M.; methodology, T.T.; software, T.T.; validation, T.T.; formal analysis, T.T.; investigation, T.T.; resources, P.M. and B.M.; data curation, T.T.; writing—original draft preparation, T.T.; writing—review and editing, T.T., P.M. and B.M.; visualisation, T.T.; supervision, P.M. and B.M.; project administration, B.M. and P.M.; funding acquisition, B.M. and P.M. All authors have read and agreed to the published version of the manuscript.

Funding: This research was funded by the Department of Science, Technology and Innovation (DSTI) of South Africa (SA) through the Collaborative Program in Additive Manufacturing (CPAM), grant number HLM4BMX.

Data Availability Statement: The original contributions presented in this study are included in the article. Further inquiries can be directed to the corresponding author.

Acknowledgments: The authors thank the Council for Scientific and Industrial Research for the laboratory equipment support. We also wish to thank Pushetso Tema from the University of Johannesburg for assisting with metallography, and Paul Lekoadi and Hosia Kgomo from CSIR for their assistance with SEM imaging.

Conflicts of Interest: The authors declare no conflicts of interest.

References

1. Song, C.; Liu, L.; Yang, Y.; Weng, C. Prediction on Geometrical Characteristics of Laser Energy Deposition Based on Regression Equation and Neural Network. In Proceedings of the IFAC-PapersOnLine, Online, 1 January 2020; pp. 89–96.
2. Theeda, S.; Jagdale, S.H.; Ravichander, B.B.; Kumar, G. Optimization of Process Parameters in Laser Powder Bed Fusion of SS 316L Parts Using Artificial Neural Networks. *Metals* **2023**, *13*, 842. [CrossRef]
3. Pardhi, Y. *Laser Metal Deposition—Developing New Materials [White Paper]*; Sulzer: Houston, TX, USA, 2022.
4. O'Neill, F.; Mehmanparast, A. A review of additive manufacturing capabilities for potential application in offshore renewable energy structures. *Forces Mech.* **2024**, *14*, 100255. [CrossRef]
5. Ehsan Toyserkani, A.K.; Stephen, F. Corbin Introduction. In *Laser Cladding*, 1st ed.; CRC Press: Boca Raton, FL, USA, 2004; pp. 1–22, ISBN 9780429121890.
6. Barekat, M.; Shoja Razavi, R.; Ghasemi, A. Nd:YAG laser cladding of Co–Cr–Mo alloy on γ-TiAl substrate. *Opt. Laser Technol.* **2016**, *80*, 145–152. [CrossRef]
7. Dalaee, M.; Cerrutti, E.; Dey, I.; Leinenbach, C.; Wegener, K. Parameters Development for Optimum Deposition Rate in Laser DMD of Stainless Steel EN X3CrNiMo13-4. *Lasers Manuf. Mater. Process.* **2022**, *9*, 1–17. [CrossRef]
8. Mostajeran, A.; Shoja-Razavi, R.; Hadi, M.; Erfanmanesh, M.; Barekat, M.; Savaghebi Firouzabadi, M. Evaluation of the mechanical properties of WC-FeAl composite coating fabricated by laser cladding method. *Int. J. Refract. Met. Hard Mater.* **2020**, *88*, 105199. [CrossRef]
9. Liu, Y.; Jiang, W.; Chen, Z.; Xu, Q.; Zhang, Z.; He, J. Optimization of processing parameters and microstructure evolution of (TiB+La_2O_3)/Ti6Al4V manufactured by laser melting deposition. *J. Mater. Res. Technol.* **2023**, *24*, 8086–8097. [CrossRef]
10. Nenadl, O.; Ocelík, V.; Palavra, A.; Hosson, J.T.M.D. The Prediction of Coating Geometry from Main Processing Parameters in Laser Cladding. *Phys. Procedia* **2014**, *56*, 220–227. [CrossRef]
11. de Oliveira, U.; Ocelík, V.; De Hosson, J.T.M. Analysis of coaxial laser cladding processing conditions. *Surf. Coat. Technol.* **2005**, *197*, 127–136. [CrossRef]
12. Erfanmanesh, M.; Abdollah-Pour, H.; Mohammadian-Semnani, H.; Shoja-Razavi, R. An empirical-statistical model for laser cladding of WC-12Co powder on AISI 321 stainless steel. *Opt. Laser Technol.* **2017**, *97*, 180–186. [CrossRef]

13. Huang, G.; Gu, D.; Dai, D.; Yuan, L.; Wang, R.; Xiong, K. Microstructure evolution and underlying thermal behavior of high-content TiC reinforced titanium matrix composites fabricated by laser directed energy deposition. *J. Mater. Res. Technol.* **2023**, *23*, 3007–3022. [CrossRef]
14. Fan, P.; Zhang, G. Study on process optimization of WC-Co50 cermet composite coating by laser cladding. *Int. J. Refract. Met. Hard Mater.* **2020**, *87*, 105133. [CrossRef]
15. Zhou, Z.; Liu, Y. New insights into the evolution of TiB whisker and TiC particle during selective laser melting of titanium matrix composites. *Mater. Sci. Eng. A Struct. Mater. Prop. Microstruct. Process.* **2023**, *877*, 145200. [CrossRef]
16. Nomqonde, B.H.; Mashinini, P.M.; Lekoadi, P.; Masina, B.N. Investigation of the microstructure evolution of TiC/Ti-6Al-4V composite manufactured by laser melting deposition. In Proceedings of the MATEC Web of Conferences, Online, 9–11 November 2022; p. 1005.
17. Wang, J.; Zeng, Y.; Fan, W.; Li, L.; Tong, Y.; Wang, Z.; Jiang, F. Microstructure and tensile properties of TiCp/Ti6Al4V composites by laser melting deposition with different dissolving degrees of TiC. *Ceram. Int.* **2022**, *48*, 34650–34657. [CrossRef]
18. Liu, Y.; Chen, Z.; He, J. Nanosized SiC particle reinforced Ti6Al4V matrix composites manufactured by laser melting deposition. *Procedia Struct. Integr.* **2022**, *42*, 1249–1258. [CrossRef]
19. Shesh, S. Additive manufacturing research and development needs. In *Additive Manufacturing Handbook*, 1st ed.; Badiru, A.B., Valencia, V.V., Liu, D., Eds.; CRC Press: Boca Raton, FL, USA, 2017; pp. 89–127, ISBN 9781482264081.
20. Gao, J.; Wu, C.; Hao, Y.; Xu, X.; Guo, L. Numerical simulation and experimental investigation on three-dimensional modelling of single-track geometry and temperature evolution by laser cladding. *Opt. Laser Technol.* **2020**, *129*, 106287. [CrossRef]
21. Li, C.; Yu, Z.B.; Gao, J.X.; Zhao, J.Y.; Han, X. Numerical simulation and experimental study on the evolution of multi-field coupling in laser cladding process by disk lasers. *Weld. World* **2019**, *63*, 925–945. [CrossRef]
22. Gao, J.; Wang, C.; Hao, Y.; Wang, X.; Zhao, K.; Ding, X. Prediction of molten pool temperature and processing quality in laser metal deposition based on back propagation neural network algorithm. *Opt. Laser Technol.* **2022**, *155*, 108363. [CrossRef]
23. Francois, M.M.; Sun, A.; King, W.E.; Henson, N.J.; Tourret, D.; Bronkhorst, C.A.; Carlson, N.N.; Newman, C.K.; Haut, T.; Bakosi, J.; et al. Modeling of additive manufacturing processes for metals: Challenges and opportunities. *Curr. Opin. Solid State Mater. Sci.* **2017**, *21*, 198–206. [CrossRef]
24. *ASTM E407-07*; Standard Practice for Microetching Metals and Alloys. ASTM International: West Conshohocken, PA, USA, 2015.
25. Nezhad, M.N.; Aboutalebi, M.R.; Seyedein, S.H.; Barekat, M. Multi-criteria optimization of processing parameters in laser cladding of $Al_{0.5}CoCrFeNiNb_{0.5}$-$Si_{0.1}$ high entropy alloy coating. *J. Mater. Res. Technol.* **2025**, *35*, 6519–6536. [CrossRef]
26. Pant, P.; Chatterjee, D. Prediction of clad characteristics using ANN and combined PSO-ANN algorithms in laser metal deposition process. *Surf. Interfaces* **2020**, *21*, 100699. [CrossRef]
27. Kennedy, J.; Eberhart, R. Particle swarm optimization. In Proceedings of the ICNN'95—International Conference on Neural Networks, Perth, Australia, 27 November–1 December 1995.
28. Miranda, L.J.V. PySwarms: A research toolkit for Particle Swarm Optimization in Python. *J. Open Source Softw.* **2018**, *3*, 433. [CrossRef]
29. Le, T.-N.; Lo, Y.-L. Effects of sulfur concentration and Marangoni convection on melt-pool formation in transition mode of selective laser melting process. *Mater. Des.* **2019**, *179*, 107866. [CrossRef]
30. Borges, B.; Quintino, L.; Miranda, R.M.; Carr, P. Imperfections in laser clading with powder and wire fillers. *Int. J. Adv. Manuf. Technol.* **2010**, *50*, 175–183. [CrossRef]
31. Zeng, Y.; Wang, J.; Wei, J.; Xue, Y.; Zhao, Z.; Tang, L.; Li, L.; Tong, Y.; Jiang, F. Microstructure and properties of inter/inner-layer regions of TiCp/Ti6Al4V composites manufactured by laser melting deposition. *Mater. Lett.* **2022**, *316*, 131989. [CrossRef]
32. Xu, D.; Wang, J.; Wang, Z.; Sun, Q.; Guo, C.; Jiang, F.; Tong, Y. Elimination of defects in laser metal deposited TiCp/Ti6Al4V composite by synchronous ultrasonic impact treatment. *Mater. Lett.* **2023**, *347*, 134635. [CrossRef]
33. Qiao, G.; Zhang, B.; Bai, Q.; Gao, Y.; Du, W.; Zhang, Y. Machinability of TiC-reinforced titanium matrix composites fabricated by additive manufacturing. *J. Manuf. Process.* **2022**, *76*, 412–418. [CrossRef]
34. Li, Y.; Song, L.; Xie, P.; Cheng, M.; Xiao, H. Enhancing Hardness and Wear Performance of Laser Additive Manufactured Ti6Al4V Alloy Through Achieving Ultrafine Microstructure. *Materials* **2020**, *13*, 1210. [CrossRef]